W^+W^-H production through bottom quarks fusion at hadron colliders

Pankaj Agrawal [a,b], Biswajit Das [a,b,*]

[a] *Institute of Physics, Sainik School Post, Bhubaneswar 751005, India*
[b] *Homi Bhabha National Institute, Training School Complex, Anushakti Nagar, Mumbai 400094, India*

ARTICLE INFO

ABSTRACT

With the standard model working well in describing the collider data, the focus is now on determining the standard model parameters as well as for any hint of deviation. In particular, the determination of the couplings of the Higgs boson with itself and with other particles of the model is important to better understand the electroweak symmetry breaking sector of the model. In this letter, we look at the process $pp \rightarrow WWH$, in particular through the fusion of bottom quarks. Due to the non-negligible coupling of the Higgs boson with the bottom quarks, there is a dependence on the $WWHH$ coupling in this process. This sub-process receives the largest contribution when the W bosons are longitudinally polarized. We compute one-loop QCD corrections to various final states with polarized W bosons. We find that the corrections to the final state with the longitudinally polarized W bosons are large. It is shown that the measurement of the polarization of the W bosons can be used as a tool to probe the $WWHH$ coupling in this process. We also examine the effect of varying $WWHH$ coupling in the κ-framework.

Contents

1. Introduction

Standard Model (SM) has been very successful. It has been tested in a wide variety of low energy and high energy experiments [1,2]. Although there is no firmly established conflict between the data and the standard model predictions, the model is not yet fully validated. In particular, the Higgs sector of the model is not yet fully explored. The Higgs potential can still have many allowed shapes [3]. Self-couplings of the Higgs boson and its couplings with some of the standard model particles are still loosely bound. The more precise measurement of the couplings can also lead to hints to beyond the standard model scenarios.

In this letter, we are interested in the coupling of the Higgs boson with the W and Z bosons (collectively referred to as V); in particular, we are interested in the quartic $VVHH$ couplings. In the standard model, the VVH and $VVHH$ couplings are related. The experimental verification of this relationship is important to
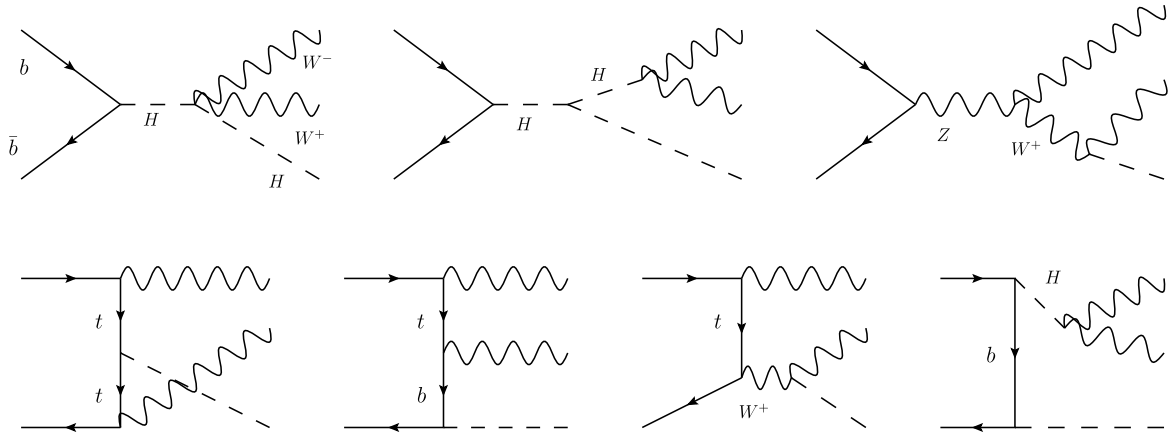
Fig. 1. A few LO Feynman diagrams for W^+W^-H production in $b\bar{b}$ channel. Diagrams in the upper row are s-channel diagrams and in the lower row are t-channel diagrams.

put the standard model on a firm footing. There are scenarios beyond the SM, where these couplings are either not related or have different relationship [4]. The ATLAS collaboration has put a bound on this coupling at the Large Hadron Collider (LHC). Using the VBF mechanism of a pair of Higgs boson, and using 126 fb^{-1} of data at 13 TeV, there is a bound of $-0.43 < \kappa_{V_2H_2} < 2.56$ at 95% confidence level [5]. Here $\kappa_{V_2H_2}$ is the scaling factor for the $VVHH$ coupling. However, in this process, the bounds on $WWHH$ and $ZZHH$ couplings cannot be separated. The process $pp \to HHV$, where a pair of Higgs bosons are produced in association with a W or a Z boson, allows us to separately measure $HHWW$ and $HHZZ$ couplings. Gluon-gluon fusion would contribute to HHZ production. This mechanism is important at HE-LHC and FCC-hh. However, dependence on the scaling of $HHVV$ coupling is weak. The expected bound from the WHH production at the HL-LHC is $-10.6 < \kappa_{V_2H_2} < 11$ [6], which is quite loose.

Instead of these processes, we consider the process $pp \to HWW$ at hadron colliders. This process can help us in measuring $HHWW$ coupling, independent of $HHZZ$ coupling. This process can take place by both quark-quark [7] and gluon-gluon scattering. At a 100 TeV collider, gluon-gluon scattering and bottom-bottom quark scattering give important contributions. These contributions depend on $HHWW$ coupling. The gluon-gluon contribution is discussed in [8]. This contribution is smaller than the contribution of bottom-bottom scattering. The contribution of bottom-bottom scattering is only about 15–20% of the light quarks scattering contribution at the 100 TeV center of mass energy (CME) and at the leading order (LO), light quarks contribution does not depend on $WWHH$ coupling. The dependence on this quartic coupling, $WWHH$, can be enhanced if we measure the polarization of the final state W bosons. There is a significant enhancement of the fraction of the bottom-bottom scattering events when both W bosons in the final states are longitudinally polarized. The ATLAS and CMS collaborations have measured the W polarization at the LHC [9–11]. We compute the one-loop QCD corrections to various combinations of final state W bosons polarization. The longitudinally polarized W boson final states receive the largest corrections, leading to even larger fraction of events with bottom-bottom scattering. We also scale the $WWHH$ coupling and examine the effect of the NLO QCD corrections and the measurement of the polarization of W bosons. It appears that an analysis of WWH events, when both the W bosons are longitudinally polarized, can help in determining the $WWHH$ coupling.

The paper is organized as follows. The second and third sections describe the process and the details of the calculations. In the fourth section, we present the numerical results and the last section has the conclusions.

2. The process

We are interested in quark-quark scattering for the production of WWH. To study $WWHH$ coupling, we consider this process in five-flavor scheme. We study the process $b\bar{b} \to W^+W^-H$ at hadron colliders. We take bottom quarks as massless but at the same time, we consider $b\bar{b}H$ Yukawa coupling which is proportional to the mass of the bottom quark. With this consideration, the diagrams with $WWHH$ coupling would appear, with the Higgs boson coupling to the bottom quark. This coupling would not appear at the leading order (LO) for the other quarks in the initial state. This channel has been discussed only with $t\bar{t}H$ Yukawa couplings [12] but not with $b\bar{b}H$ Yukawa couplings.

At the LO, there are 20 diagrams – 9 s-channel and 11 t-channel. A representative set of diagrams is displayed in Fig. 1. Only one of the diagrams has $WWHH$ coupling which is one of our main points of interest. We vary $WWHH$ coupling in order to see its impact on the cross section for the different center of mass energies. There is no strong coupling dependency in the LO diagrams; they solely depend on electroweak couplings. Some of the t-channel diagrams depend on $t\bar{t}H$ Yukawa couplings and give large contributions to the LO cross section, due to the top-quark mass dependency of $t\bar{t}H$ Yukawa coupling.

To compute the one-loop QCD corrections to this process, we need to include one-loop diagrams and next-to-leading order (NLO) tree level diagrams. The one-loop diagrams can be categorized as pentagon, box, triangle as well as bubble diagrams. There are 3 pentagon diagrams, 14 box diagrams, 34 triangle diagrams, and 14 bubble diagrams. A few representative NLO diagrams are displayed in Fig. 2. There is only one triangle diagram that has $WWHH$ coupling. Bubble diagrams are UV divergent and a few triangle diagrams are also UV divergent. To remove UV divergence from the amplitude, counterterm (CT) diagrams need to be added to the virtual amplitudes. There are 15 vertex CT diagrams and 14 self energy CT diagrams. A set of CT diagrams are shown in Fig. 3. Also, most of the virtual diagrams are infrared (IR) singular. In order to remove IR singularities from the virtual diagrams, one needs to include real emission diagrams. There are three such processes. These processes are a) $b\bar{b} \to W^+W^-Hg$, b) $g\bar{b} \to W^+W^-H\bar{b}$ and c) $bg \to W^+W^-Hb$. There are 54 Feynman diagrams for each of these processes. We have shown a few diagrams for the first subprocess in Fig. 3. All these diagrams have been generated using a `Mathematica` package, `FeynArts` [13].

3. Calculations and checks

We have to perform $2 \to 3$ and $2 \to 4$ tree level and $2 \to 3$ one loop calculations. For the calculation, we use helicity methods.
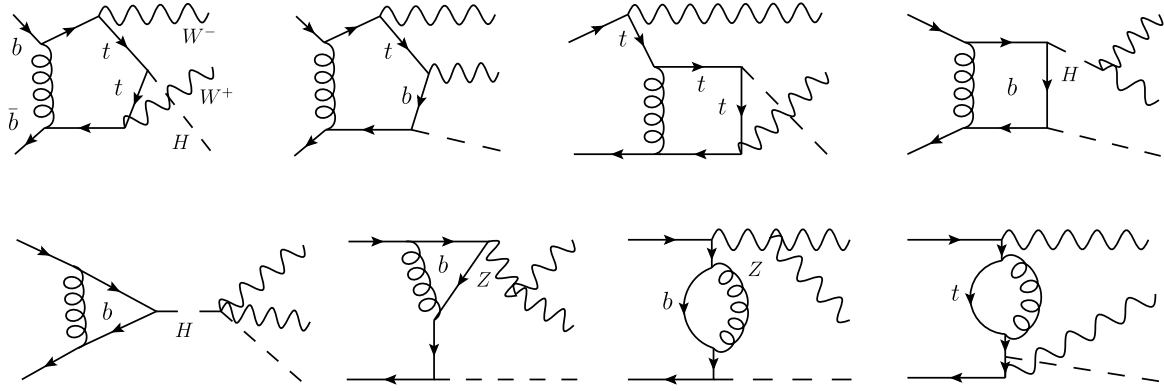
Fig. 2. A few sample one-loop Feynman diagrams for W^+W^-H production in $b\bar{b}$ channel.
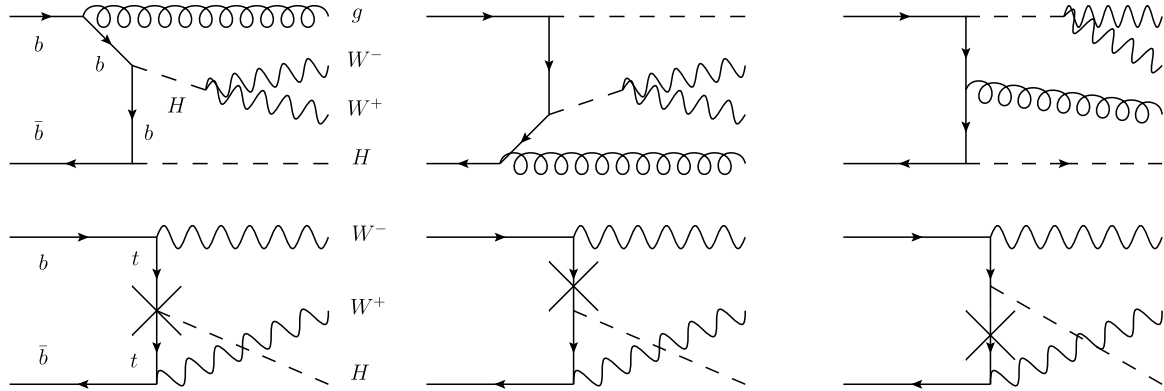

Fig. 3. A few sample real emission Feynman diagrams for the sub-process $b\bar{b} \to W^+W^-H\,g$ and vertex CT diagrams and self energy CT diagrams for the process $b\bar{b} \to W^+W^-H$.

As a starting point, we consider a few prototype diagrams in each case. With suitable crossing and coupling choices, we can compute the rest of the diagrams. We compute helicity amplitudes at the matrix element level for the prototype diagrams. These helicity amplitudes can be used to probe the physical observables dependent on the polarization of external particles. As mentioned before, the b-quarks are treated as massless quarks because of their small mass and we use massless spinors for b-quarks. The tree level helicity amplitudes can be written in terms of the spinor products $\langle pq \rangle$ and $[pq]$ [14]. For one-loop amplitudes, we use an extra object - the vector current $\langle p\gamma^\mu q \rangle$. We take the functional form of the spinor products $\langle pq \rangle$ or $[pq]$ from Ref. [15] and we extend their treatment to calculate the functional form of the vector current $\langle p\gamma^\mu q \rangle$. We have checked that the calculated $\langle p\gamma^\mu q \rangle$ satisfies various spinor identities. We adopt four-dimensional-helicity (FDH) scheme [16,17] to compute the amplitudes. In this scheme, all spinors, γ-matrices algebra are computed in 4-dimensions. We use package FORM [18] to implement the helicity formalism. In this calculation, we don't have fermion loops; so there are no traces of matrices involving γ_5. Therefore in our scheme, we have treated γ_5 with properties same as that in four-dimension [19,20].

Using FORM, we write helicity amplitude in terms of spinorial objects, scalar products of momenta and polarizations. For the one-loop calculations, we also have tensor and scalar integrals. The one-loop scalar integrals are computed using the package OneLoop [21]. We use an in-house reduction code, OVReduce [22,23], to compute tensor integrals in dimensional regularization. Finally, the phase space integrals have been done with the advanced Monte-Carlo integration (AMCI) package [24]. In AMCI, the VEGAS [25] algorithm is implemented using parallel virtual machine (PVM) package [26].

Few checks have been performed to validate the amplitudes. The one-loop amplitudes have both ultraviolet (UV) and infrared (IR) singularities. UV singularities are removed by using counterterm (CT) diagrams and the IR divergences are removed using Catani-Seymour (CS) dipole subtraction methods. The cancellation of these divergences are powerful checks on the calculation. All UV singularities are removed by fermionic mass and wave function renormalization. There are no UV singularities coming from pentagon and box diagrams as there are no 4-point box tensors in those amplitudes. UV singularities are coming from the triangle as well as bubble diagrams. The appropriate vertex and self energy counterterms (CT) diagrams have been added in total amplitude which gives renormalized amplitude. A few sample CT diagrams are depicted in Fig. 4. We use the $\overline{\text{MS}}$ scheme for massless fermions and the on-shell subtraction scheme for massive fermions.

The next check is infrared (IR) singularity cancellation. We implement the Catani-Seymour dipole subtraction method [27] for the cancellation of IR singularities. Except bubble diagrams, all other virtual diagrams are IR singular. Collectively all IR singularities coming from virtual diagrams cancel with IR singularities coming from real emission diagrams.

Following the Catani-Seymour method, the NLO cross section can be written as

$$\sigma^{NLO} = \int_{m+1} d\sigma^R + \int_m d\sigma^V$$

$$= \int_{m+1} (d\sigma^R - d\sigma^A) + \int_m \left(d\sigma^V + \int_1 d\sigma^A \right), \tag{3.1}$$
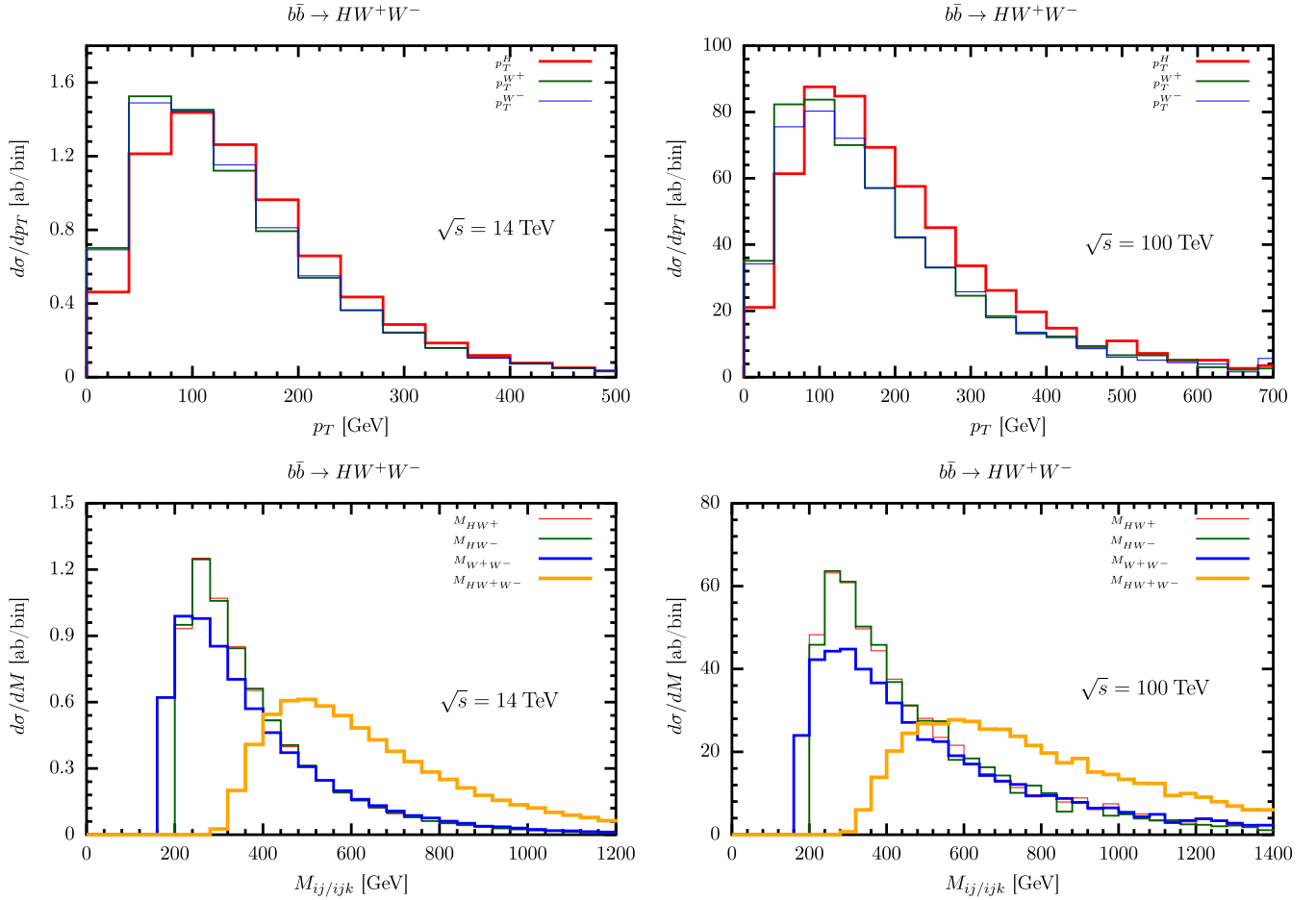
Fig. 4. The NLO differential cross section distribution with respect to transverse momentum (p_T) and invariant masses ($M_{ij/ijk}$) for 14 and 100 TeV CMEs.

where $d\sigma^R$, $d\sigma^V$ and $d\sigma^A$ are exclusive cross section, one-loop virtual correction and approximation term respectively. $d\sigma^A$ has the same pointwise singular behavior as $d\sigma^R$ and hence behaves as a local counterterm for $d\sigma^R$ and then first integration can be performed safely in $\epsilon \to 0$ limits. The second term of the second integral will give dipole I term which will remove all the infrared singularities from virtual correction and add a finite contribution. The dipole I factor comes from analytical integration of $d\sigma^A$ in d-dimensions over one-parton phase space. It can be written as

$$\int_1 d\sigma^A = d\sigma^B \otimes I, \tag{3.2}$$

where $d\sigma^B$ is the born level cross section and the symbol $\otimes$ describes phase space convolution and sum over spin and color indices. The term $d\sigma^B \otimes I$ is evaluated over the rest of the m-parton phase space and cancels all singularities from renormalized virtual amplitudes. As discussed before, we use the FDH scheme, so we take I term in the FDH scheme. The term I given in Ref. [27] is in conventional dimensional regularization (CDR) scheme and in any other regularization scheme (RS), it is given as [28]

$$I^{\mathrm{RS}}(\{p\}, \epsilon) = I^{\mathrm{CDR}}(\{p\}, \epsilon) - \frac{\alpha_s}{2\pi} \sum_I \widetilde{\gamma}_I^{\mathrm{RS}} + \mathcal{O}(\epsilon). \tag{3.3}$$

In the FDH scheme, $\widetilde{\gamma}_I^{\mathrm{RS}}$ are

$$\widetilde{\gamma}_q^{\mathrm{FDH}} = \widetilde{\gamma}_{\bar{q}}^{\mathrm{FDH}} = \frac{1}{2} C_F, \quad \widetilde{\gamma}_g^{\mathrm{FDH}} = \frac{1}{6} C_F. \tag{3.4}$$

Now with this I term, we have checked that the integration in the second term of Eq. (3.1) is IR safe. Also, there are other terms in the dipole subtraction method, called P and K terms which will add finite contributions to σ^{NLO}. These terms come from the factorization of initial-state singularities into parton distribution functions. The color operator algebra, explicit forms of $V_{ij,k}$, I, P and K are given in Ref. [27].

There are three real emission sub-processes that can contribute to σ^{NLO}. These processes are

a) $b\,\bar{b} \to W^+ W^- H\,g$ b) $g\,\bar{b} \to W^+ W^- H\,\bar{b}$

c) $b\,g \to W^+ W^- H\,b$, \hfill (3.5)

as these processes mimic the Born level process in soft and collinear regions. Due to large contributions, top resonance in the last two processes jeopardizes the perturbative calculation. The cross sections for these two processes are five to six times higher than the Born level cross section. One cannot remove those top resonant diagrams as it will affect the gauge invariance and we have checked that the interference between resonant and non-resonant diagrams coming from the off-shell region is large which will again ruin the perturbative computations. There are several techniques to remove these on-shell contributions safely [29–32]. One can also restrict resonant top momenta out of the on-shell region and can have contribution only from the off-shell region. To implement the last technique with a standard jet veto, one needs a very large number of phase space points to get a stable cross section. The implementation of these techniques is beyond the scope

Table 1

The LO and NLO cross sections for different collider CMEs with their respective scale uncertainties. RE is the relative enhancement of the total cross section from the Born level cross section.

CME (TeV)	σ^{LO} [ab]	σ^{NLO}_{QCD} [ab]	RE
14	$217^{+16.1\%}_{-18.9\%}$	$289^{+17.6\%}_{-20.8\%}$	33.2%
27	$1086^{+19.2\%}_{-20.5\%}$	$1559^{+18.0\%}_{-20.8\%}$	43.6%
100	$15258^{+22.0\%}_{-20.9\%}$	$23097^{+20.6\%}_{-21.0\%}$	51.4%

of this paper. Instead, we exclude the last two channels by assuming b-quark tagging with 100% efficiency [12,33].

4. Numerical results

The sub-process $b\bar{b} \rightarrow W^+W^-H$ gives a significant contribution to the main process $pp \rightarrow W^+W^-H$. We calculate the NLO QCD contribution to this process. In particular, we focus on the corrections to cross sections and distributions for various polarization configurations of the final state particles. We also probe variation of cross sections with $WWHH$ anomalous coupling. Some of the Feynman diagrams, tree-level diagrams, as well as one-loop diagrams are heavy vector bosons, Higgs boson and top quark mediated. We use complex-mass scheme (CMS) [34] throughout our calculation to handel the resonance instabilities coming from these massive unstable particles. We take Weinberg angle as $cos^2\theta = (m_W^2 - i\Gamma_W m_W)/(m_Z^2 - i\Gamma_Z m_Z)$. The input SM parameters are [35]: $m_W = 80.385$ GeV, $\Gamma_W = 2.0854$ GeV, $m_Z = 91.1876$ GeV, $\Gamma_Z = 2.4952$ GeV, $m_H = 125$ GeV, $\Gamma_H = 0.00407$ GeV, $m_t = 173.2$ GeV, $\Gamma_t = 1.44262$ GeV. For the bottom-quark mass, we have used the running mass, as we have renormalized bottom quark mass in $\overline{\text{MS}}$ scheme. We have used $m_b = 2.8$ GeV which can be obtained by running the mass $m_b = 4.92$ GeV at bottom mass scale to the Higgs boson mass scale [36]. We have used this value for both LO and the NLO calculations. For the top quark, we have renormalized in on-shell scheme. There are several pieces in the one-loop calculation which contribute to total σ^{NLO}. As we have discussed above, virtual amplitudes, CT amplitudes, dipole ***I***, ***P*** and ***K*** terms, dipole subtracted real emission amplitudes contribute to the finite part. We find that there are significant contributions from all these pieces except dipole subtracted real emission amplitudes which gives an almost vanishing contribution.

We use `CT14lo` and `CT14nlo` PDF sets [37] for LO (σ^{LO}) and NLO (σ^{NLO}) cross sections calculation. We use these PDF sets through `LHAPDF` [38] libraries. As mentioned before, we calculate the cross sections in three different CMEs corresponding to current and proposed future colliders. We choose renormalization (μ_R) and factorization (μ_F) scales dynamically as

$$\mu_R = \mu_F = \mu_0$$
$$= \frac{1}{3}\left(\sqrt{p_{T,W^+}^2 + M_W^2} + \sqrt{p_{T,W^-}^2 + M_W^2} + \sqrt{p_{T,H}^2 + M_H^2} \right),$$
(4.1)

where $p_{T,W}$, $p_{T,H}$ are the transverse momenta and M_W, M_H are the masses of W and Higgs bosons. We measure the scale uncertainties by varying both μ_R and μ_F independently by a factor of two around the μ_0 given in Eq. (4.1).

4.1. Results for the SM

We have listed the cross sections for different CMEs with their respective scale uncertainties in Table 1. As we see in Table 1 the LO cross sections are 217, 1086 and 15258 *ab*, whereas NLO cross sections are 289, 1559 and 23097 *ab* at 14, 27 and 100 TeV

CMEs respectively. The cross section rapidly increases with CME as PDFs for b-quarks are small for lower energies. The relative enhancements $\left(RE = \frac{\sigma^{NLO}_{QCD} - \sigma^{LO}}{\sigma^{LO}} \right)$ due to NLO QCD correction are also presented in that table. The RE also increases with CME and it is 33.2%, 43.6% and 51.4% for 14, 27 and 100 TeV CMEs respectively. We have calculated scale uncertainty as the relative change in the cross sections for the different choices of scales within bound $0.5\mu_0 \leq \mu_R/\mu_F \leq 2\mu_0$. We see that the NLO uncertainties are a little bit higher than the LO. As there is no strong coupling (α_s) at the Born level, the LO uncertainties come from the factorization scale whereas at the NLO the uncertainties come from both, factorization as well as renormalization scales. To see the different scale uncertainties separately, we vary μ_R and μ_F independently. We see the renormalization scale uncertainty varies from $\sim -11\%$ to $\sim 0.7\%$ and the factorization scale varies from $\sim -15.7\%$ to $\sim 17.3\%$ at NLO depending on CMEs from 14 to 100 TeV.

To get a better understanding, let us consider the diagrams in Fig. 1, which make contributions at the LO. These diagrams can be classified into four categories – 1) The diagrams with one bottom-Yukawa coupling, 2) the diagrams with one top-Yukawa coupling, 3) the diagrams without these Yukawa couplings, 4) The diagrams with two bottom-Yukawa couplings. At the tree level, because of a change of helicity at the Yukawa vertex, the diagrams of the first category do not interfere with the other three categories. The second and fourth categories of diagrams are t-channel diagrams. They have the same helicity structure as the third category of diagrams. The diagrams with two bottom-Yukawa couplings make a very small contribution. The main contribution comes from the individual square of the matrix elements of the first three categories. In particular, the square of matrix elements of the second and third categories are individually quite large, but there is also a sizable destructive interference between these two categories of diagrams. At the NLO level, in addition, we need to include contributions of the interference between the LO order diagrams and one-loop diagrams. The relative contribution of these terms is discussed below.

As discussed before, we probe the contributions from different polarization configurations of the final state W bosons to the LO and NLO cross sections. The right-handed, left-handed and longitudinal polarization of a W boson are denoted as '+', '–', and '0'. The contributions of different nine polarization combinations of final state W bosons are given in Table 2 for 14, 27 and 100 TeV CMEs. We see that the large contributions are coming from the longitudinal polarization states and among them, the '00' combination gives the largest contribution to the total cross sections. Relative enhancement (RE) for the '00' combination increases with the CME and it becomes $\sim 117\%$ at 100 TeV. In the R_ξ gauge, the pseudo Goldstone bosons couple to massive fermions with a coupling proportional to the mass of the fermion. These pseudo Goldstone bosons represent the longitudinal polarization state of a W boson. This leads to larger values of the cross section in longitudinal polarization combinations due to heavy fermion mediated diagrams. These longitudinal polarization modes are useful for background suppression to this process. The background may come from the processes with gauge bosons or gluons or photons couplings with light quarks. The negligible masses of the light quarks (u, d, s and c) lead to the suppression of backgrounds in polarization combinations that include longitudinal polarization.

At the 100 TeV CME, the NLO corrections are largest for '00' combination of W boson polarization. In this case, the largest positive contribution comes from the interference of the second category LO diagrams and one-loop diagrams corresponding to the third category and vice-versa. But the interference of second category LO diagrams and corresponding one-loop diagrams is negative; the same is true for the interference of the third category

Table 2

The LO and NLO cross sections and their relative enhancements (RE) for different polarization combinations of final state W bosons and their sum at 14, 27 and 100 TeV CMEs. The results are in *ab* unit.

Pol. com.	14 TeV			27 TeV			100 TeV		
	σ^{LO}	σ_{QCD}^{NLO}	RE (%)	σ^{LO}	σ_{QCD}^{NLO}	RE (%)	σ^{LO}	σ_{QCD}^{NLO}	RE (%)
++	13	18	38.5	60	88	46.7	702	1056	50.4
+−	18	25	38.9	82	127	54.9	965	1499	55.3
+0	37	49	32.4	187	266	42.2	2568	3336	29.9
−+	4	6	50.0	19	28	47.4	229	334	45.9
−−	13	18	38.5	61	89	45.9	707	1044	47.7
−0	22	28	27.3	108	144	33.3	1454	1346	−7.4
0+	22	28	27.3	109	145	33.0	1470	1216	−17.3
0−	37	49	32.4	186	268	44.1	2583	3151	22.0
00	51	67	31.4	274	404	47.4	4490	9748	117.1
$\sum$	217	289	32.2	1086	1559	43.6	15258	23097	51.4

Table 3

The LO and NLO cross sections in 4FNS and the $b\bar{b}$ channel at 14 and 100 TeV CMEs. The results for 4FNS have been obtained using `MagGraph5_aMC5@NLO`. The $b\bar{b}$ channel results are from our code.

channel	14 TeV		100 TeV	
	σ^{LO} [ab]	σ_{QCD}^{NLO} [ab]	σ^{LO} [ab]	σ_{QCD}^{NLO} [ab]
4FNS	9460	13250	108100	185100
$b\bar{b}$	217	289	15258	23097

LO diagrams and corresponding one-loop diagrams. A small positive contribution is also obtained from the interference of the first category LO diagrams and corresponding one-loop diagrams. These diagrams are responsible for the $WWHH$ coupling dependence of the process.

To find the relative contribution of the bottom-bottom scattering to the $pp \rightarrow W^+W^-H$ process, we compute the cross sections in other $q\bar{q}$ channels along with the $b\bar{b}$ channel. The results are presented in Table 3. The cross sections in $q\bar{q}$ channels (4FNS) have been calculated using `MagGraph5_aMC5@NLO` [39]. `Mag-Graph5_aMC5@NLO` cannot compute the one-loop QCD corrections to the $b\bar{b}$ channel due to the presence of the resonances in the diagrams. As we see in Table 3, the $b\bar{b}$ channel gives significant contributions to the full process $pp \rightarrow W^+W^-H$. The $b\bar{b}$ channel contributes $\sim 2.3\%$ to the LO and $\sim 2.1\%$ to the NLO cross sections at 14 TeV and $\sim 14.1\%$ to the LO and $\sim 12.5\%$ to the NLO cross sections at 100 TeV of process $pp \rightarrow W^+W^-H$. These numbers are calculated without the channels $gg \rightarrow W^+W^-H$, which can also add a significant contribution to the process $pp \rightarrow W^+W^-H$ [8,12]. If one adds gg channel, these numbers will be changed accordingly. As we see in Table 3, the corrections are pretty high in $q\bar{q}$ channels (4FNS). In those channels, `Mad-Graph5_aMC@NLO` includes all real emission diagrams and the results are complete but we impose a jet veto on b-quarks with 100% efficiency for real emission diagrams to overcome certain difficulties discussed in Sec. 3. The proper inclusion of all real emission diagrams may increase the QCD correction significantly in the $b\bar{b}$ channel.

We have plotted a few different kinematical distributions at the NLO level in Fig. 4 and Fig. 5. In Fig. 4, the upper-panel histograms are for the transverse momentum (p_T) of final state particles at 14 and 100 TeV CMEs. As expected p_T distributions of W bosons almost coincide with each other. The p_T distribution of the Higgs boson is a bit harder. The differential cross sections are maximum around $p_T = 100$ TeV for the Higgs boson and near $p_T = 80$ TeV for the W bosons. In the lower panel of Fig. 4, we have plotted the histograms for the different invariant masses ($M_{ij,ijk}$) at 14 and 100 TeV CMEs. Invariant mass thresholds are around ~ 210, ~ 170, ~ 290 TeV and distributions are peaked around 250, 230,

490 TeV for M_{HW}, M_{WW} and M_{HWW} respectively. In Fig. 5, we have plotted differential cross sections with respect to the rapidity (η) of final state particles and cosine angle ($\cos\theta$) between the two final state particles for 100 TeV CME. The distributions have maxima around $\eta = 0$, -0.4 and 0.4 for the Higgs boson, W^+ and W^- boson respectively. From the $\cos\theta$ plot in Fig. 5, it is clear that maximum contributions come when two final state particles are near to collinear region i.e., $\theta \sim 0$ or π. In Fig. 6, we have plotted the LO and the NLO distributions to show the effect of the one-loop QCD corrections. The distributions are for only 100 TeV CME. The behavior for the 14 TeV CME is similar. In the upper half of Fig. 6, p_T distributions are plotted and in the lower half of Fig. 6, invariant masses have been plotted at 100 TeV CME. We see an increase for the smaller values of the kinematic variables in all the plotted distributions.

4.2. Anomalous coupling effect

As we discussed in the introduction, $VVHH$ coupling in SM is only loosely bound so far. We allow $WWHH$ coupling to deviate from the SM value in the search for new physics in the context of κ-framework [40,41]. In the κ framework, only SM couplings deviate by a scale factor. κ is defined as the deviation from the SM coupling. It is a scale factor. Although WWH and $WWHH$ couplings in the SM are related but in many Effective Field Theory frameworks, these couplings can vary independently [4]. As there is no QCD correction to $WWHH$-vertex, the anomalous coupling will not affect the renormalization. We have checked that the UV and IR poles cancel with the same CTs and dipole terms as in the SM. We denote deviation of $VVHH$ coupling from the SM as $\kappa_{V_2H_2}$ and $\kappa_{V_2H_2} = 1$ in the SM. In this framework, we vary $\kappa_{V_2H_2}$ from -2.0 to 2.0 and calculate the relative increment $\left(\text{RI} = \frac{\sigma_\kappa - \sigma_{\text{SM}}}{\sigma_{\text{SM}}}\right)$ in the total cross section, whereas the κ for other SM couplings are set to 1. We choose $\kappa_{V_2H_2} = -2.0$, -1.0, 1.5, 2.0 and tabulate the results for the LO and NLO cross sections at 14 and 100 TeV CMEs in Table 4. It is clear from Table 4 that cross sections are lower than SM prediction when $\kappa_{V_2H_2}$ is positive and higher than the SM predictions when $\kappa_{V_2H_2}$ is negative. (We note that this is due to the interference pattern within the diagrams of the first category.) There is not a significant relative increment (-0.3 to $+2.1\%$) at 14 TeV. At 100 TeV, relative increment varies from -2.2% to $+11.4\%$ for the LO cross section and from -2.1% to $+10.3\%$ for the NLO cross section. There is also HHH coupling involved in this process. We also observe the HHH anomalous coupling effect on the total cross sections. We vary corresponding κ_{H_3} from 0.5 to 2.0. We see that there is no significant change in the LO as well as the NLO cross sections and relative increase are smaller than 1% for 14 and 100 TeV CMEs. We see something very interesting in Table 5. The cross sections for the two longitudinally polarized W
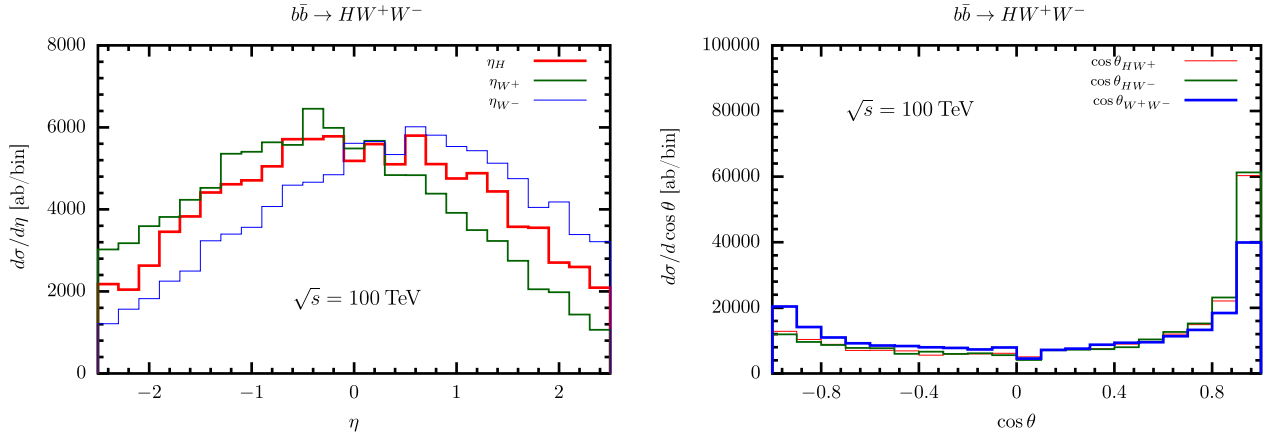
Fig. 5. The NLO differential cross section distribution with respect to rapidity (η) and cosine angle ($\cos\theta$) between the two final state particles at 100 TeV CME. Plots for 14 TeV are similar.
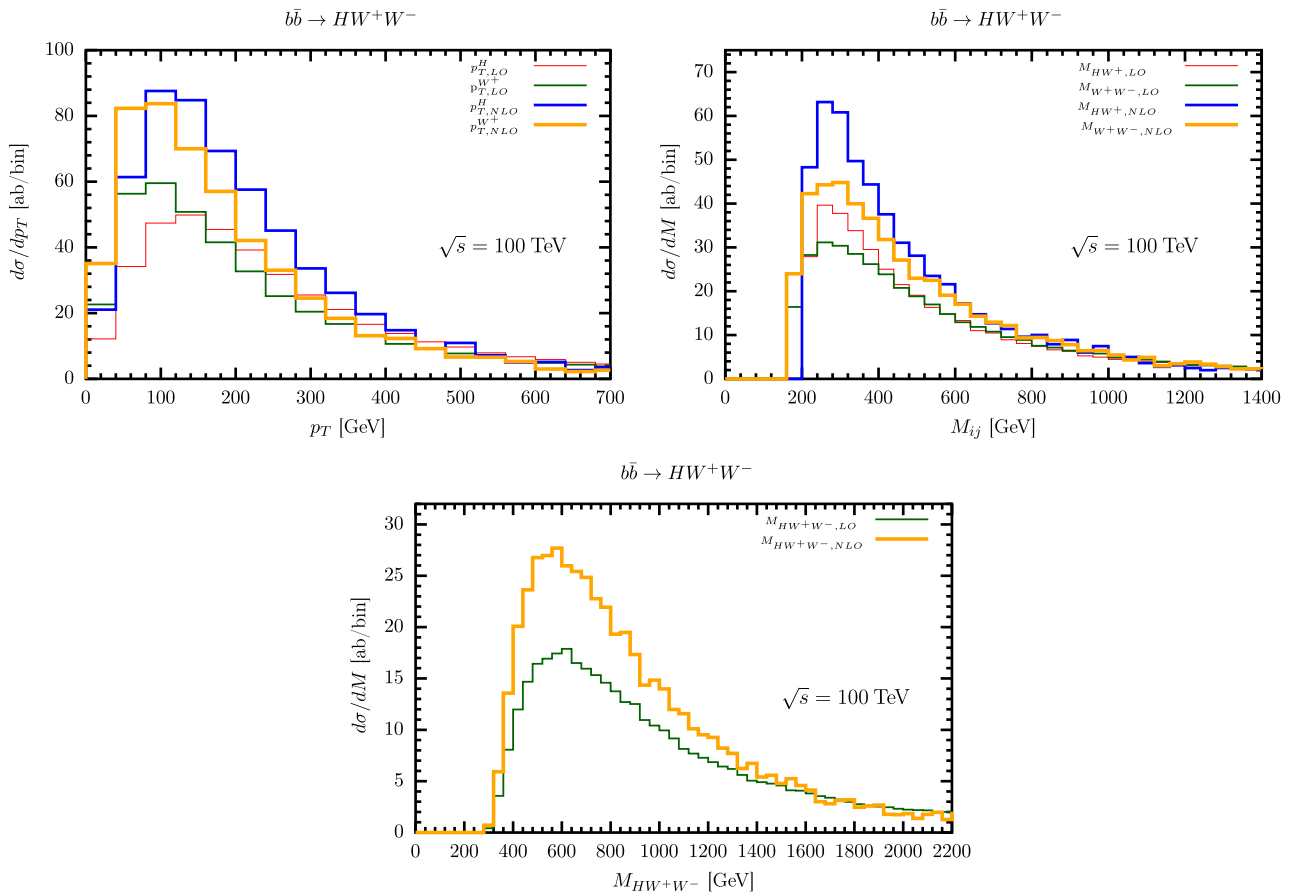

Fig. 6. The LO and NLO differential cross section distribution with respect to transverse momentums (p_T) and invariant masses ($M_{ij/ijk}$) for 100 TeV CME.

bosons configuration have a stronger dependence on the $\kappa_{V_2H_2}$. For the NLO cross sections, the dependence is almost twice as strong as in the total cross sections. This again demonstrates the importance of measuring the polarization of the W bosons. However, this dependence is weaker as compared to the LO cross sections. The difference in this dependence underlines the importance of considering the NLO corrections.

In Fig. 7, we have plotted the NLO differential cross section distributions for the Higgs boson and W^+ boson transverse momenta and different invariant masses. The maxima of the differential cross sections are about at the same value as for the SM. As there is not that much increase for $\kappa_{V_2H_2} = 2$, the corresponding

distributions nearly overlap with the SM. On the other hand, we see a sharp deviation in distributions from the SM for $\kappa_{V_2H_2} = -2$. An interesting fact about the negative $\kappa_{V_2H_2}$ is that the distributions are harder. This difference in the shape can be used in putting a strong bound on the coupling. One could put a cut on p_T^W, or one of the plotted invariant masses to select events with a larger component of anomalous events.

5. Conclusion

In this letter, we have focused on the NLO QCD corrections to $b\bar{b} \to WWH$. This process has significant dependence on $WWHH$
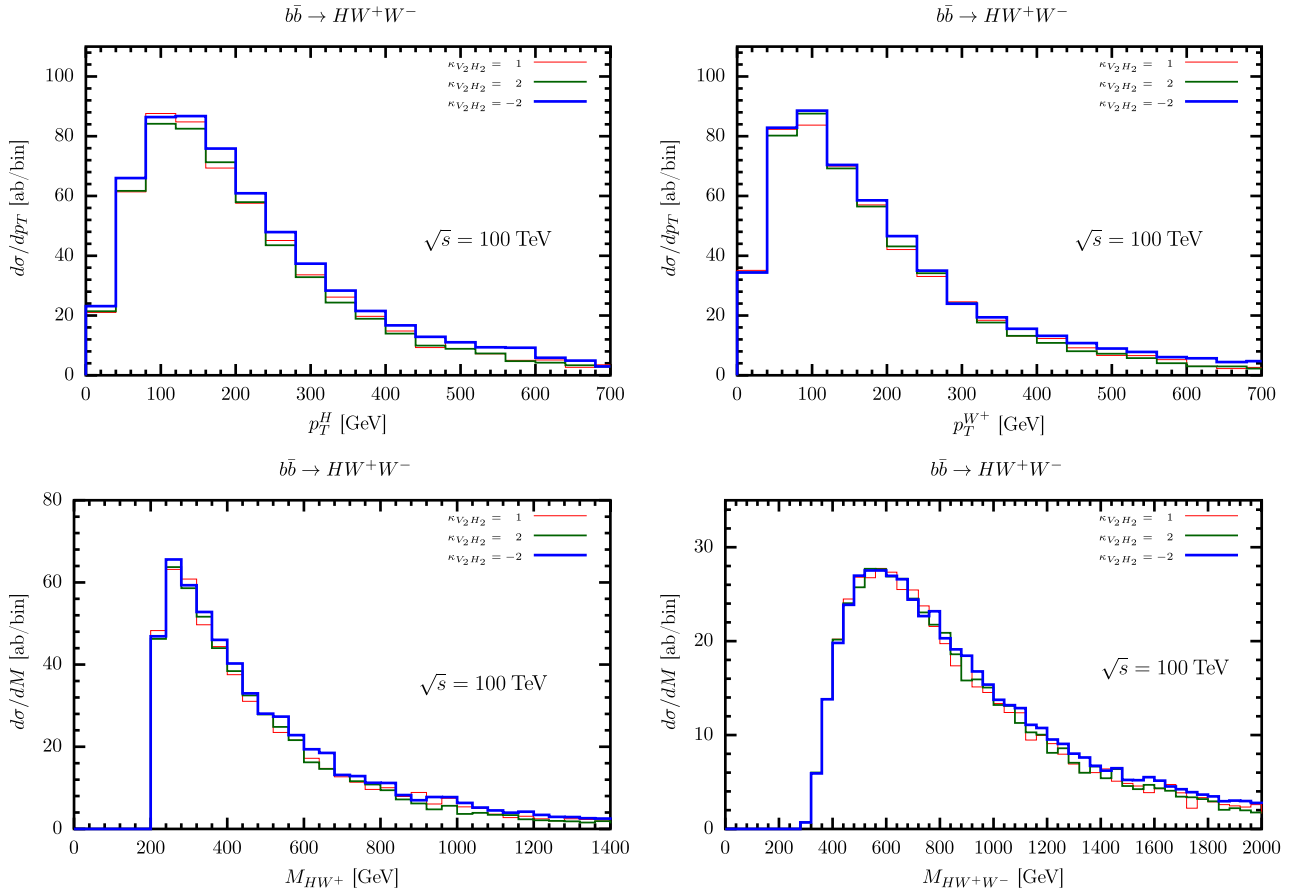
Fig. 7. Effect of anomalous $VVHH$ coupling on differential cross section distribution at 100 TeV CME. Upper panel plots are for the transverse momentum of Higgs boson (p_T^H) and W^+ boson ($p_T^{W^+}$). Lower panel plots are for the $H - W^+$ (M_{HW^+}) and $H - W^+ - W^-$ ($M_{HW^+W^-}$) invariant masses.

Table 4

Effect of anomalous $WWHH$ coupling on the LO and NLO cross sections at the 14 and 100 TeV CMEs.

CME (TeV)	$\kappa_{V_2H_2}$	σ^{LO}[ab]	RI	σ^{NLO}[ab]	RI
	1.0 (SM)	217		289	
14	2.0	216	[−0.5%]	288	[−0.3%]
	1.5	216	[−0.5%]	289	[0.0%]
	−1	220	[+1.4%]	293	[+1.4%]
	−2.0	222	[+2.3%]	295	[+2.1%]
	1.0 (SM)	15258		23097	
100	2.0	14925	[−2.2%]	22607	[−2.1%]
	1.5	15048	[−1.4%]	22810	[−1.2%]
	−1.0	16296	[+6.8%]	24760	[+7.2%]
	−2.0	16997	[+11.4%]	25465	[+10.3%]

Table 5

Effect of anomalous $VVHH$ coupling on '00' mode at 100 TeV CME.

$\kappa_{V_2H_2}$	σ^{LO}[ab]	RI	σ^{NLO}[ab]	RI
1.0 (SM)	4490		9748	
2.0	4159	[−7.4%]	9544	[−2.1%]
1.5	4333	[−3.5%]	9654	[−1.0%]
−1.0	5493	[+22.3%]	11117	[+14.0%]
−2.0	6164	[+37.2%]	11993	[+23.0%]

coupling. But, the contribution of this process to $pp \to WWH$ is only about 15–20% of that of light quark scattering. This is where the consideration of the polarization of the W bosons helps. When both the W bosons are longitudinally polarized, then this fraction can increase to about 50%. It turns out that the NLO QCD correc-

tions are also largest for this polarization configuration, making the dependence on the $WWHH$ coupling even stronger. For example, at the 100 TeV CME, the NLO corrections are about 51%, but the corrections are about 117%, when both final state W bosons are longitudinally polarized. Our study suggests that the measurement of the polarization of the final state W/Z bosons can be a useful tool to measure the couplings of the vector bosons and Higgs boson. We have also examined the effect of the variation of $\kappa_{V_2H_2}$. The variation in the cross section can be twice as large when we consider longitudinally polarized W bosons. In addition, we find that the invariant mass and the p_T^W distributions are considerably harder for the negative values of $\kappa_{V_2H_2}$. This can also be useful to put a stronger bound on the coupling. However, to find the bound, one would need to do a detailed background analysis which we leave for the future.

Declaration of competing interest

Acknowledgements

References

[1] K. Monig, Highlights and perspectives from the ATLAS experiment, in: The Large Hadron Collider Physics Conference, 25–30 May 2020.

[2] P. Mcbride, Highlights and perspectives from the CMS experiment, in: The Large Hadron Collider Physics Conference, 25–30 May 2020.

[3] P. Agrawal, D. Saha, L.-X. Xu, J.-H. Yu, C.P. Yuan, Determining the shape of the Higgs potential at future colliders, Phys. Rev. D 101 (2020) 075023, arXiv:1907.02078.

[4] F. Bishara, R. Contino, J. Rojo, Higgs pair production in vector-boson fusion at the LHC and beyond, Eur. Phys. J. C 77 (2017).

[5] G. Aad, B. Abbott, D.C. Abbott, A. Abed Abud, K. Abeling, D.K. Abhayasinghe, et al., Erratum to: search for the $hh \rightarrow b\bar{b}b\bar{b}$ process via vector-boson fusion production using proton-proton collisions at $\sqrt{s} = 13$ TeV with the atlas detector, J. High Energy Phys. 2021 (2021).

[6] K. Nordström, A. Papaefstathiou, VHH production at the high-luminosity LHC, Eur. Phys. J. Plus 134 (2019) 288, arXiv:1807.01571.

[7] J. Baglio, Next-to-leading order QCD corrections to associated production of a SM Higgs boson with a pair of weak bosons in the POWHEG-BOX, Phys. Rev. D 93 (2016) 054010, arXiv:1512.05787.

[8] P. Agrawal, D. Saha, A. Shivaji, Di-vector boson production in association with a Higgs boson at hadron colliders, arXiv:1907.13168.

[9] CMS collaboration, S. Chatrchyan, et al., Measurement of the polarization of W bosons with large transverse momenta in W+jets events at the LHC, Phys. Rev. Lett. 107 (2011) 021802, arXiv:1104.3829.

[10] ATLAS collaboration, G. Aad, et al., Measurement of the W boson polarization in top quark decays with the ATLAS detector, J. High Energy Phys. 06 (2012) 088, arXiv:1205.2484.

[11] ATLAS collaboration, M. Aaboud, et al., Measurement of $W^{\pm}Z$ production cross sections and gauge boson polarisation in pp collisions at $\sqrt{s} = 13$ TeV with the ATLAS detector, Eur. Phys. J. C 79 (2019) 535, arXiv:1902.05759.

[12] J. Baglio, Gluon fusion and $b\bar{b}$ corrections to $HW^{+}W^{-}/HZZ$ production in the POWHEG-BOX, Phys. Lett. B 764 (2017) 54, arXiv:1609.05907.

[13] T. Hahn, Generating Feynman diagrams and amplitudes with FeynArts 3, Comput. Phys. Commun. 140 (2001) 418, arXiv:hep-ph/0012260.

[14] M.E. Peskin, Simplifying multi-jet QCD computation, in: 13th Mexican School of Particles and Fields, vol. 1, 2011, arXiv:1101.2414.

[15] R. Kleiss, W. Stirling, Cross-sections for the production of an arbitrary number of photons in electron - positron annihilation, Phys. Lett. B 179 (1986) 159.

[16] Z. Bern, D.A. Kosower, The computation of loop amplitudes in gauge theories, Nucl. Phys. B 379 (1992) 451.

[17] C. Gnendiger, et al., To d, or not to d: recent developments and comparisons of regularization schemes, Eur. Phys. J. C 77 (2017) 471, arXiv:1705.01827.

[18] J. Vermaseren, New features of FORM, arXiv:math-ph/0010025.

[19] H.-S. Shao, Y.-J. Zhang, K.-T. Chao, Dijet invariant mass distribution in top quark hadronic decay with QCD corrections, Phys. Rev. D 84 (2011) 094021, arXiv:1106.5483.

[20] C. Gnendiger, A. Signer, γ_5 in the four-dimensional helicity scheme, Phys. Rev. D 97 (2018) 096006, arXiv:1710.09231.

[21] A. van Hameren, OneLOop: for the evaluation of one-loop scalar functions, Comput. Phys. Commun. 182 (2011) 2427, arXiv:1007.4716.

[22] P. Agrawal, A. Shivaji, Di-vector boson + jet production via gluon fusion at hadron colliders, Phys. Rev. D 86 (2012) 073013, arXiv:1207.2927.

[23] P. Agrawal, G. Ladinsky, Production of two photons and a jet through gluon fusion, Phys. Rev. D 63 (2001) 117504, arXiv:hep-ph/0011346.

[24] S. Veseli, Multidimensional integration in a heterogeneous network environment, Comput. Phys. Commun. 108 (1998) 9, arXiv:physics/9710017.

[25] G. Lepage, A new algorithm for adaptive multidimensional integration, J. Comput. Phys. 27 (1978) 192.

[26] A. Geist, A. Beguelin, J. Dongarra, W. Jiang, R. Manchek, V.S. Sunderam, PVM: A Users' Guide and Tutorial for Network Parallel Computing, MIT Press, 1994, 11.

[27] S. Catani, M. Seymour, A general algorithm for calculating jet cross-sections in NLO QCD, Nucl. Phys. B 485 (1997) 291, arXiv:hep-ph/9605323.

[28] S. Catani, M. Seymour, Z. Trocsanyi, Regularization scheme independence and unitarity in QCD cross-sections, Phys. Rev. D 55 (1997) 6819, arXiv:hep-ph/9610553.

[29] M. Grazzini, S. Kallweit, S. Pozzorini, D. Rathlev, M. Wiesemann, $W^{+}W^{-}$ production at the LHC: fiducial cross sections and distributions in NNLO QCD, J. High Energy Phys. 08 (2016) 140, arXiv:1605.02716.

[30] A. Denner, S. Dittmaier, S. Kallweit, S. Pozzorini, NLO QCD corrections to off-shell top-antitop production with leptonic decays at hadron colliders, J. High Energy Phys. 10 (2012) 110, arXiv:1207.5018.

[31] F. Cascioli, S. Kallweit, P. Maierhöfer, S. Pozzorini, A unified NLO description of top-pair and associated Wt production, Eur. Phys. J. C 74 (2014) 2783, arXiv:1312.0546.

[32] T. Gehrmann, M. Grazzini, S. Kallweit, P. Maierhöfer, A. von Manteuffel, S. Pozzorini, et al., $W^{+}W^{-}$ production at hadron colliders in next to next to leading order QCD, Phys. Rev. Lett. 113 (2014) 212001, arXiv:1408.5243.

[33] A. Bierweiler, T. Kasprzik, J.H. Kühn, S. Uccirati, Electroweak corrections to W-boson pair production at the LHC, J. High Energy Phys. 11 (2012) 093, arXiv:1208.3147.

[34] A. Denner, S. Dittmaier, The complex-mass scheme for perturbative calculations with unstable particles, Nucl. Phys. B, Proc. Suppl. 160 (2006) 22.

[35] M. Grazzini, S. Kallweit, M. Wiesemann, J.Y. Yook, $W^{+}W^{-}$ production at the LHC: NLO QCD corrections to the loop-induced gluon fusion channel, Phys. Lett. B 804 (2020) 135399.

[36] R.V. Harlander, W.B. Kilgore, Higgs boson production in bottom quark fusion at next-to-next to leading order, Phys. Rev. D 68 (2003) 013001, arXiv:hep-ph/0304035.

[37] S. Dulat, T.-J. Hou, J. Gao, M. Guzzi, J. Huston, P. Nadolsky, et al., New parton distribution functions from a global analysis of quantum chromodynamics, Phys. Rev. D 93 (2016) 033006, arXiv:1506.07443.

[38] M. Whalley, D. Bourilkov, R. Group, The Les Houches accord PDFs (LHAPDF) and LHAGLUE, in: HERA and the LHC: A Workshop on the Implications of HERA and LHC Physics (Startup Meeting, CERN, 26-27 March 2004; Midterm Meeting, CERN, 11-13 October 2004), vol. 8, 2005, pp. 575–581, arXiv:hep-ph/0508110.

[39] J. Alwall, R. Frederix, S. Frixione, V. Hirschi, F. Maltoni, O. Mattelaer, et al., The automated computation of tree-level and next-to-leading order differential cross sections, and their matching to parton shower simulations, J. High Energy Phys. 07 (2014) 079, arXiv:1405.0301.

[40] LHC Higgs Cross Section Working Group collaboration, A. David, A. Denner, M. Duehrssen, M. Grazzini, C. Grojean, G. Passarino, et al., LHC HXSWG interim recommendations to explore the coupling structure of a Higgs-like particle, arXiv:1209.0040.

[41] M. Ghezzi, R. Gomez-Ambrosio, G. Passarino, S. Uccirati, NLO Higgs effective field theory and κ-framework, J. High Energy Phys. 07 (2015) 175, arXiv:1505.03706.